Pedestal properties of negative triangularity discharges in ASDEX Upgrade

B. Vanovac[1], M. Dunne[2], T. Pütterich[2], T. Happel[2], J. Hobirk[2], D. Silvagni[2], M. Faitsch[2], K. Lee[2,3], G. D. Conway[2], R. Bielajew[1], C. Yoo[1], A. E. White[1], M. Bernert[2], P. David[2], R. Fischer[2], D. Stieglitz[2], the ASDEX Upgrade Team*, and the EUROfusion WPTE team**

[1]Plasma Science and Fusion Center, Massachusetts Institute of Technology, Cambridge, MA 02139, USA

[2]Max-Planck-Institut für Plasmaphysik, 85748 Garching, Germany

[3]University of Science and Technology, Daejeon, Republic of Korea

*See author list of H. Zohm et al, 2024 Nucl. Fusion https://doi.org/10.1088/1741-4326/ad249d

**See E. Joffrin et al, Overview of the EUROfusion Tokamak Exploitation programme in support of ITER and DEMO, Nuclear Fusion 2024 10.1088/1741-4326/ad2be4

E-mail: vanovac@mit.edu

Abstract.

In this work, we explore pedestal properties of negative triangularity discharges with upper triangularity of $\delta_u \approx -0.35$ and with both ion ∇B drift direction. In all cases, the discharges undergo a transition to H-mode with accompanying edge localized modes that are not explained by the peeling-ballooning stability analysis alone. A variation with the ion ∇B drift direction is observed. A lower pressure gradient, shallower radial electric field well and increased temperature fluctuations are measured in favorable case. In addition, irregular edge localized modes are present. This difference is more pronounced in ECRH heated plasmas compared to plasmas with combined NBI and ECRH. A comparative analysis between two discharges, featuring similar plasma parameters but varied shaping, suggest that an interplay between other parameters such as magnetic shear, the timing of the auxiliary heating and shaping, might play a strong role in low to high confinement transitions. While the low shaping discharge maintained L-mode, the high shaping discharge entered H-mode with edge localized modes, contrary to expectations.

1. Introduction

Currently, prospects of successfully burning plasma in a tokamak device rely on plasma operation with an edge transport barrier (ETB) in high confinement mode (H-mode). The ETB provides a pedestal that elevates core density and temperature profiles and consequently improves core confinement. However, due to the steep gradients forming in this edge region, the ETB periodically relaxes when the pedestal pressure and associated current density exceeds an MHD limit known as the ideal peeling-ballooning (PB) boundary [1]. Crossing this limit causes periodic excursions of heat and particles out of the confined plasma and towards the plasma-facing components and is shown to be one of the main limitations towards long-lasting divertors in larger machines [2, 3]. Those periodic relaxations of the pedestal are called type-I Edge-Localized Modes (ELMs) [4]. Multiple ELM-free regimes, resulting from the tailoring of the pedestal profiles, have been developed. This includes actively suppressing and mitigating ELMs using magnetic

perturbation coils [5]. Others, like the Enhanced D-Alpha (EDA-H modes) regime [6], Improved energy confinement mode (I-mode) [7], and Quasi-continuous exhaust (QCE) regime [8] - have naturally absent or mitigated ELMs. In those cases the transport is increased in the pedestal region, which maintains the pedestal profiles below the PB boundary. Many studies have been made on ELM-free regimes and are summarized in an overview paper [9].

An alternative approach to enhanced confinement without experiencing ELMs involves modifying the equilibrium of the plasma. Specifically, adjustments in plasma shaping, such as flipping the "D" shape of the plasma to achieve what is referred to as *negative triangularity* (NT), have demonstrated improved core confinement and operation without encountering the edge transport barrier. Notably, current experiments conducted in TCV [10] and DIII-D [11] have successfully achieved enhanced confinement without the typical pedestals associated with H-mode operation. Instead, they have achieved an L-mode-like plasma edge with significant reductions in transport [12, 13, 14]. Numerical simulations have demonstrated limitations in distinctly capturing the reduction in turbulence levels attributed solely to triangularity. While reductions in ion-scale turbulence due to trapped electron modes (TEM) have been observed in both linear and non-linear simulations at TCV [15], no preferential triangularity sign was identified for the reduction of heat flux driven by ion-temperature-gradient (ITG) modes, as reported in [16]. The heat flux was observed to decrease for both positive and negative triangularity, provided the triangularity was sufficiently pronounced. In contrast, simulations reported in [17], which utilized the same magnetic equilibrium as [16], indicated the opposite: triangularity was found to increase the transport level regardless of its sign, with a stronger effect observed for positive triangularity. Currently, there is no coherent understanding of the effect of triangularity on ITG in the plasma core, necessitating more refined numerical analyses. In the edge region, the unstable high toroidal mode number ballooning modes have been proposed as the mechanism preventing access to H-modes below a certain triangularity value δ [18] and recent experiments with sufficiently shaped diverted plasma at DIII-D have shown that type-I ELM avoidance can be achieved over a wide range of parameters as long as δ remains below a critical threshold [19] $\delta < \delta_{crit}$. These results demonstrate the successful integration of core and edge effects simultaneously, positioning negative triangularity as a potentially viable operating scenario for a burning plasma [20, 21, 22, 23].

Figure 1 shows important geometrical parameters in the poloidal cross section of a tokamak plasma for calculating upper (δ_u) and lower (δ_l) triagnularity, defined as:

$$\delta_u = (R_{geo} - R_{zmax})/a \qquad and \qquad \delta_l = (R_{geo} - R_{zmin})/a. \tag{1}$$

where a is the minor radius of the plasma defined as $(R_{out} - R_{in})/2$, R_{geo} is the geometric major radius defined as $(R_{in} + R_{out})/2$. R_{zmax} and R_{zmin} are the radii of the highest and the lowest vertical points of the separatrix and R_{in} and R_{out} are the inner and the outer most radial points of the plasma boundary. In addition, the average triangularity

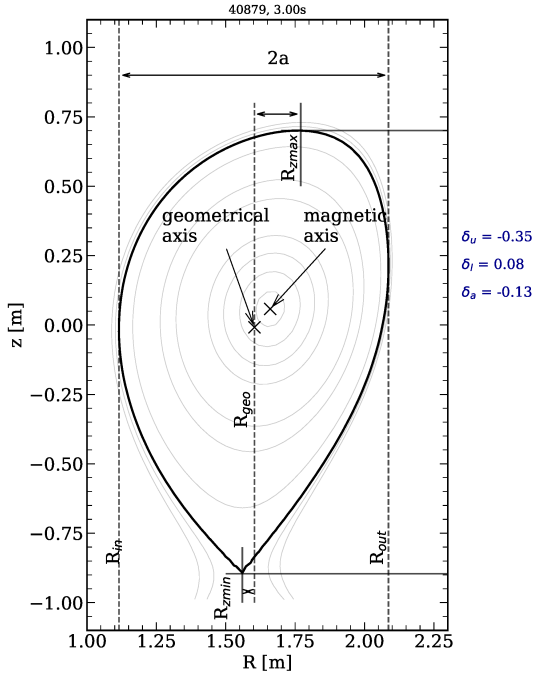

Figure 1. The poloidal cross section of the plasma geometry with shaping parameters relevant for calculating the triangularity, as defined in [24]. This shape is from plasma discharge # 40879 performed at 800 kA of plasma current. Shaping parameters such as upper (δ_u), lower (δ_l) and average triangularity (δ_a) are displayed.

is defined as :

$$\delta_{av} = \frac{\delta_u + \delta_l}{2} \tag{2}$$

s described in [25], to ensure the L-mode operation in NT, the safest is to keep the X-point δ sufficiently negative. In addition, in [25] and references herein, the non-X-point δ (i.e. the upper δ in a lower single null (LSN) configuration) has been identified as the most important one for confinement improvement. In this manuscript, alongside the upper triangularity, we use the average triangularity as defined in equation 2 where equal weight is given to both lower and the upper triangularities. An additional shaping caveat is that, as pointed out in [26], ASDEX Upgrade NT plasmas undergo a degree of tilting of the ellipsoidal flux surface with respect to the z-axis. This can influence plasma performance. However, in this work the degree of tilt has not been considered since the compared discharges have the same shaping and, therefore, the same tilt.

In this work, the sign of the magnetic field is varied in the same plasmas to reverse the ion ∇B drift, consequently increasing the L to H-mode (LH) power threshold when the ion ∇B drift directions points away from the active X-point. When operating in unfavorable drift, to keep the helicity, a change of the plasma current direction is applied accordingly, and all discharges were performed in LSN configuration. When operating

in favorable ion grad B drift direction, the NBI injection is co-current, while when operating in unfavorable configuration, the NBI is counter-current.

In the ASDEX Upgrade tokamak, which features a tungsten wall, initial investigations have revealed that the critical factor for preventing H-mode access in NT is the operation with reversed field where the ion ∇B drift points away from the active X-point, and is known to be unfavorable for H-mode entrance [26]. The work reported in this manuscript compares two pairs of discharges performed in both favorable and unfavorable drift directions and, as will be demonstrated, they all eventually transitioned into H-modes accompanied by ELMs. Furthermore, in order to probe the LH transition, a comparison between low and high shaping discharges are presented. General ELM characteristics are shown in Section 4 and implications and further steps are discussed in section 5 of this manuscript.

2. Attempts to avoid H-modes in NT

2.1. Operation in unfavorable ion ∇B drift with only ECRH heating

In the course of NT experiments, H-mode was regularly obtained in fav. drift, even at low heating and the deep radial electric field confirms the H-mode picture of those discharges as will be shown later in the manuscript (i.e. figure 15). To increase the H-mode power threshold, the direction of the magnetic field was reversed, consequently reversing the ion ∇B drift direction. The result of this exercise is shown in figure 2 where two discharges with different magnetic field directions are shown: #40473 in blue with the ion ∇B drift direction pointing towards the active X-point (favorable) and #40870 away from the active X-point in orange (unfavorable). The discharges are designed to be identical with the only difference being the reversed I_p & B_t directions. Identical ECRH heating power steps are applied to both as shown in 2 (a) in solid colored lines. The resulting radiated power, calculated from the bolometric reconstruction [27], for the two cases is displayed in dashed lines with the higher radiated power appearing in favorable case, likely due to increased tungsten concentration. The origin of the higher tungsten concentration in the favorable case, despite the same fuelling levels and the closeness to boronization is likely due to differences in divertor and SOL conditions, which are, at present, not well diagnosed in NT plasmas. Neutral beam injection (NBI) blip, the black solid line in figure 2 (a), is applied for ion temperature measurements obtained using charge exchange recombination spectroscopy (CXRS).

As the first heating power step is applied, the forward field discharge enters into an H-mode at t = 2.56 s at total auxiliary power $P_\mathrm{ECRH} = 1.66$ MW, which can be seen as the onset of strong spikes on the bolometer signal in figure 2 (b) corresponding to the onset of ELMs. The bolometer signal recorder in unfav. drift (orange trace) remains quiet at the matching heating power level and increases after the second power step is applied, at t $\approx$ 2.9 s and P = 2.2 MW. At this point, the discharge with unfav. drift direction enters H-mode. In both discharges, the LH transition occurs during the shaping (δ) ramp

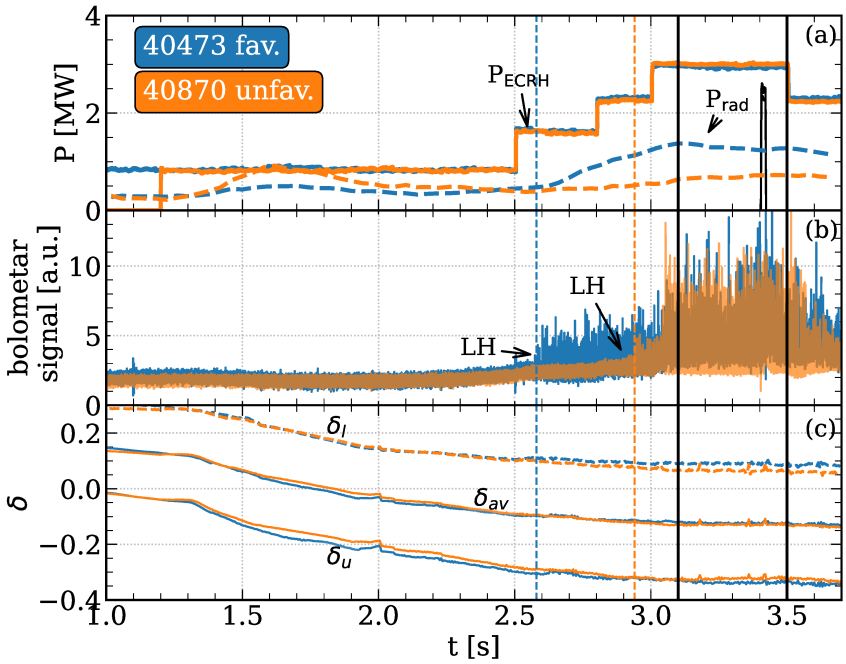

Figure 2. Time histories of fav.(blue) and ufav.(orange) discharges of relevant plasma parameters: a) identical ECRH heating power steps shown in solid lines. Radiation power from the main chamber is shown in dashed lines. Black line displays the NBI beam blip used for measurements of T_i b) A bolometer diode signal where the onset of strong spikes corresponds to ELMs where the LH transition times are marked with vertical dashed lines and LH arrows on the bolometer signal. c) Upper (dashed lines) and lower (solid lines) triangularity. The vertical solids lines encompasses a steady state time interval used in the analysis.

and is marked with vertical dashed lines. Temporal evolution of shaping is displayed in figure 2 (c) where δ_l is the lower triangularity, δ_u is the upper triangularity and δ_{av} is the average triangularity. Both discharges settle into steady state ELMy phases at the highest heating power level of P = 2.9 MW and upper triangularity of δ_u = -0.33. The confinement factor H_{98} during the steady state phase is slightly higher for favorable ($H_{98} \approx 0.9$) compared to unfavorable discharge ($H_{98} \approx 0.8$) and is not shown here. As demonstrated, both discharges enter H-mode before the final plasma shaping is reached and this might have been facilitated by the application of an early ECRH heating.

The profiles of the electron temperature (T_e [keV]), electron density (n_e [$10^{19}\mathrm{m}^{-3}$]), electron pressure (p_e [kPa]) and the ion temperature (T_i [keV]) are shown in figure 3. The profiles are obtained using an integrated data analysis (IDA) approach combining ECE, Thomson scattering (TS) for the electron temperature, and TS and Li beam diagnostics for the electron density [28]. Ion temperatures are obtained from the charge exchange measurements using the NBI beam blip and the locations of those measurements were verified using the forward model which incorporates realistic CXRS geometry and utilized the existing NBI neutral density model to model the CXRS spectra along the

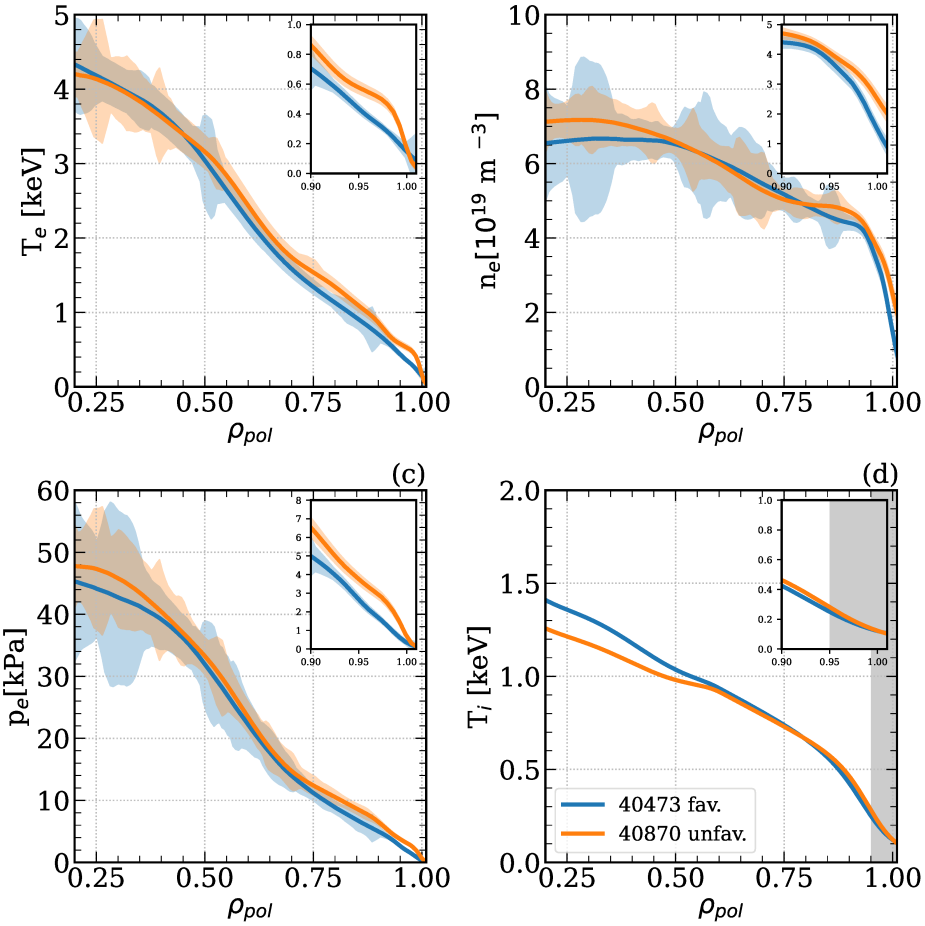

Figure 3. Profiles of the (a) electron temperature (T_e [keV]), (b) electron density (n_e [10^{19}m^{-1}]), (c) electron pressure (p_e [kPa]) and (d) the ion temperature (T_i [keV]) compared between the two discharges # 40473 H-mode (blue) and #40870 H-mode (orange)with different ion grad B drift. Insets in each figure zoom in on the edge region in between ρ_{pol} = 0.90-1.01. The gray rectangle in T_i profiles shows the region where the error bars are too large to reliably constrain the profile shape, due to non-optimized geometry of the lines of sight when measuring in negative triangulatiry shapes. Profiles are averaged over the 3.1 -3.5 s time interval.

lines of sight. The details on the development, validation and application of this forward model are described in [29]. The profiles are obtained during the steady state phase averaged over ELMs, enclosed with two solid black vertical lines in figure 2, at matched heating power levels and compared between favorable # 40473 H-mode in blue and unfavorable #40870 H-mode in orange. The same heating and fuelling power levels result in a similar core performance. At the edge, however, the electron temperature pedestal forms in unfavorable discharge while, the favorable discharge remains L-mode like as displayed in the inset of figure 3 (a). Nevertheless, both phases are clearly in H-mode as evidenced by the edge radial electric field profiles shown in figure 15 and discussed later in the manuscript. The edge electron density is slightly higher in the unfavorable case resulting in a higher edge pressure and this difference is clearly visible in the inset of figure 3 (c). The T_i data, shown in 3 (d) are similar between the two

discharges although the resolution in the very edge is not sufficient due to non-optimized geometry of NT discharges for edge measurements.

As shown in figure 2, both discharges have ELMs and their behavior is compared in figure 4. While the favorable drift is characterized by irregular bursts, as shown in figure 4 (a), the ELM behavior in unfav. drift direction is regular and typical of type-I ELM appearance. There is, as of yet, no clear explanation for such a difference in frequency patterns of ELMs, however, one potential reason could be the stronger edge density barrier in the unfav. discharge providing a more edge bootstrap current. In addition, there are no systematic fav./unfav. comparisons of ELMs at the same heating power in positive triangularity. In negative triangularity, there are indications that the regularity of ELMs depends on the closeness to the LH transition, however, understanding this behavior of ELMs is left for future work. Interestingly, this behavior is also present in the pair of mixed ECRH and NBI heated discharges as will be shown later in the manuscript.

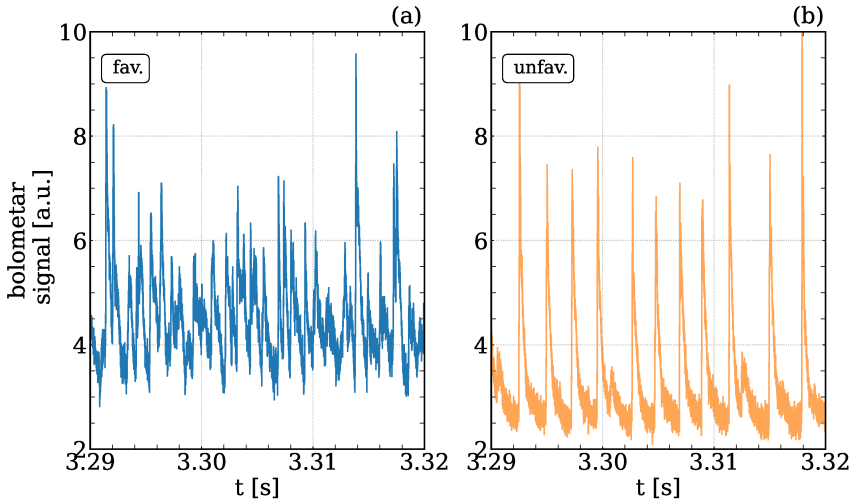

Figure 4. Time traces of bolometer signal (XVR S0L0A01) showing typical temporal evolution of ELMs during power matched phases in fav. (a) and unfav. (b) drift.

The ideal PB stability analysis is shown in figure 5 where the relationship between critical pressure gradient $\alpha_{\max}$ and current density j_{tor} across the pedestal is shown. The symbols correspond to the operational states during the phase between two spikes in bolometer signal for each discharge: blue for favorable conditions and orange for unfavorable conditions. The solid lines illustrate the computed stability boundaries using the method described in [30] and the errorbars correspond to 15 % error estimate on experimental input. Although ELM frequency increases with power in those discharges suggesting type-I ELMy behavior, the experimental points for both drift directions are significantly far from the ideal PB stability limit. The situation where the ELMs are triggered before hitting the PB stability is reminiscent of resistive ELMs, as observed in JET [31, 32]. In addition, the experimental pressure gradient in the

favorable case is much lower compared to unfavorable suggesting additional transport mechanism across the pedestal in fav. drift with ECRH heating.

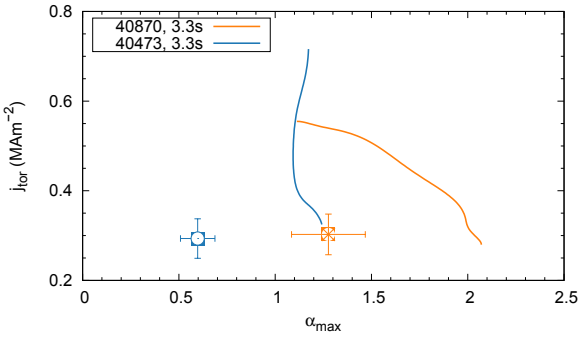

Figure 5. Ideal PB stability diagram for pure ECRH heated cases evaluated at the pre-ELM time points for forwards field direction case shown in blue and the reversed field in orange. The symbols correspond to the experimental points in terms of the maximum pressure gradient and the current density while their respective stability boundaries, calculated with the linear MHD code, are shown in solid lines.

In addition to the macroscopic MHD picture of the pedestal in favorable and unfavorable drift, we look into the turbulence behavior. Turbulence characteristics in the electron temperature channel are provided through the correlation ECE (CECE) measurements, which are sensitive to the electron temperature fluctuations given the sufficient optical depth [33, 34, 35, 36]. When the optical depth falls below a critical value, we refer to the radiative temperature fluctuations since the signals become sensitive to the presence of density fluctuations. The conditions with low optical depth are usually met very close to the separatrix region. The correlation ECE system in ASDEX Upgrade [37, 38] used for those measurements consists of 24 radially separated, but closely spaced channels. The spatial separation is within the radial correlation lengths of turbulence features. The CECE system measures the ion-scale turbulence with low radial wave vectors k, while the high-k, electron scale structures are non-accessible. The cross-correlation method of the neighboring channels ensures decorrelation of the inherent thermal noise and correlation of turbulent features.

Figure 6 shows the coherency spectra obtained with the CECE system at four radial locations spanning the outer core region towards the separatrix. Color coding corresponds to the two different drift directions. Additionally, temperature fluctuation levels are given at each location. The temperature fluctuations at the inner most measured location of $\rho_{\mathrm{pol}} = 0.85$ are $0.87\,\% \pm 0.07\,\%$ in favorable compared to $0.75\,\% \pm 0.09\,\%$ in unfavorable discharge. Inside the pedestal top at $\rho_{\mathrm{pol}} = 0.92$, the same trend continues with slightly higher temperature fluctuation levels in the favorable discharge. In the steep gradient region, at $\rho_{\mathrm{pol}} = 0.98$, δT_{rad} in forward field exceeds that of reversed field due to the strong broadband feature visible in the coherency spectra between 5 and 200 kHz. An increase in the coherency values above the noise level and between the 5 -200 kHz is visible inside the pedestal top at radial location

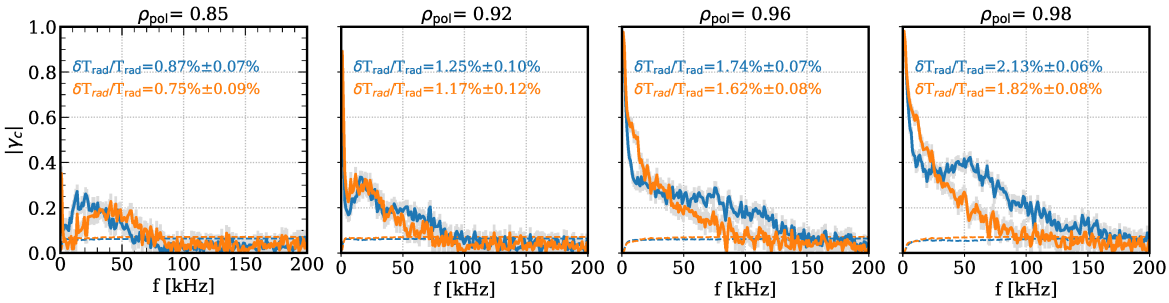

Figure 6. Coherency values calculated for the discharges # 40473 in blue (fav.) and # 40870 in orange (unfav.) at four different radial locations measured with the correlation ECE diagnostic. Relative radiative temperature fluctuation levels are displayed at each location and for the two configurations, and are calculated integrating the coherency levels between 5 - 200 kHz.

$\rho_{\mathrm{pol}} = 0.91$ suggesting its radial extent across the entire pedestal. Correlation between the stronger temperature fluctuations across the pedestal and low pedestal pressure gradient in forward drift suggests the potential role of those fluctuations in keeping the pedestal away from its ideal PB stability limit.

2.2. Operation in unfavorable ion ∇B drift with mixed NBI and ECRH heating

So far, we compared NT plasmas with purely electron heating by ECRH where, in addition, an NBI blip was applied to allow CXRS measurements of T_{i}. In the following, we compare a pair of discharges where both ECRH and NBI heating methods are applied. With an increased fraction of NBI heating the $T_{\mathrm{i}}/T_{\mathrm{e}}$ ratio is increased. As in the previous comparison, this pair of discharges is designed to be identical between fav. and unfav. drift direction and in figure 7 the favorable configuration is displayed in dark blue and unfavorable is displayed in red. The time traces of the heating power steps are shown in 7 (a) with ECRH and NBI trajectories shown as solid lines, and the radiation from the main chamber as a colored dashed lines. After switching on the NBI, the fav. discharge enters H-mode at $\mathrm{t} = 2.5\,\mathrm{s}$ and $\mathrm{P} = 1.6\,\mathrm{MW}$ as can be seen from the bolometer signal shown in 7 (b) while in the reverse field an H-mode entry is delayed until $\mathrm{t} = 2.71\,\mathrm{s}$ at $\mathrm{P} = 4\,\mathrm{MW}$. The confinement factors, H_{98}, displayed in 7 (c) settles to the same value once steady state at the highest heating power levels of 7 MW is achieved. Furthermore, in 7 (d) displays the edge electron density for both cases with identified LH transition times. In addition, the fuelling levels in D/s, equal for both discharges, is shown. The final state is the same for both forward and reversed field, however, due to different ion ∇B drift, the time histories of the H-mode entry are different.

The resulting T_{e}, n_{e}, p_{e} and T_{i}, profiles, averaged over the steady ELMy phase during the time interval between 3.1 - 3.5 s, at the highest matching heating power levels, are shown in figure 8. They are compared between forward # 40470 H-mode (blue) and reversed field # 40869 H-mode (red). The same heating and fuelling (in figure 7 (d)) schemes result in the similar core electron temperatures shown in figure 8 (a) as was

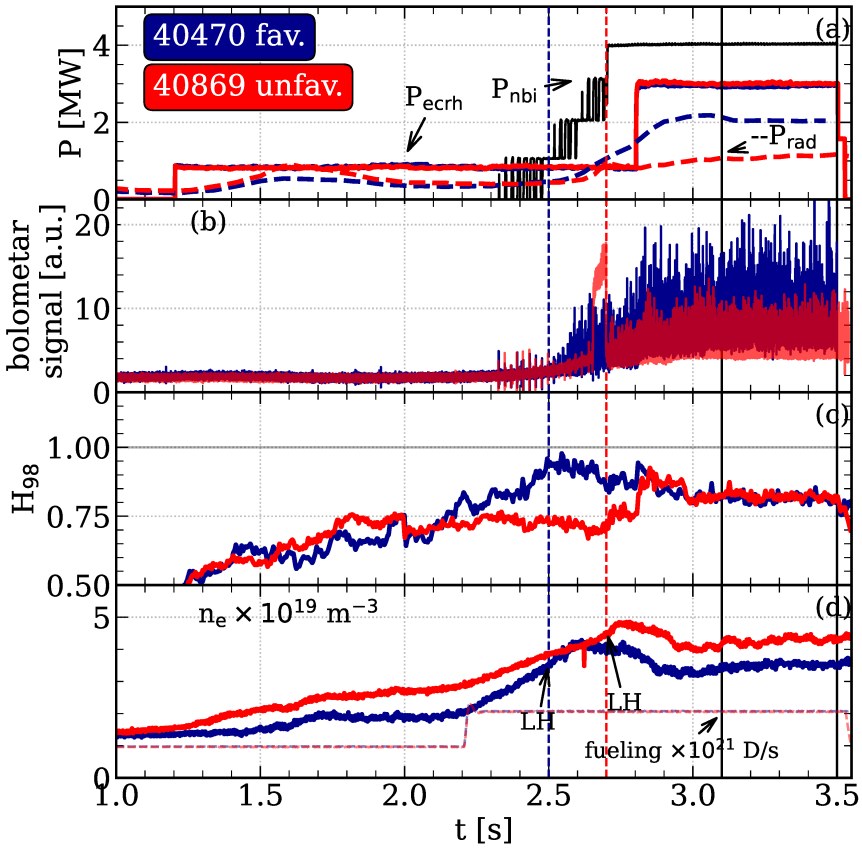

Figure 7. Time histories of favorable (blue) and unfavorable (red) discharges of relevant plasma parameters: a) NBI and ECRH heating power steps (the same in two discharges) are shown in solid lines. Radiation power from the main chamber is shown in dashed lines. b) The bolometer diode signal crossing the divertor as ELM monitor. c) Confinement factor H_{98}. d) The edge electron density n_e in slid lines with LH transition times is shown together with the fueling levels (in D/s) which were the same in both discharges, shown in dashed lines. LH transitions for both discharges are marked in vertical dashed lines.

observed in the ECRH case shown in figure 3(a). The profile shapes of the electron density are different, with higher electron density across the entire plasma radius 8 (b) in the unfavorable case. The resulting electron pressure is also higher in the unfavorable case. The T_i is larger across the plasma radius in the favorable case. The behavior of ELMs between the favorable and the unfavorable configurations is compared in figure 9. While ELMs in the favorable case are bursty, as shown in figure 9 (a), the ELM behavior in unfavorable drift direction is very regular and well-defined as shown in 9 (b) and could be due to the stronger edge density barrier in the unfav. discharge providing a more edge bootstrap current, as was the case with the ECRH heated plasmas. The frequency trend is the same trend as observed in the ECRH heated cases shown in

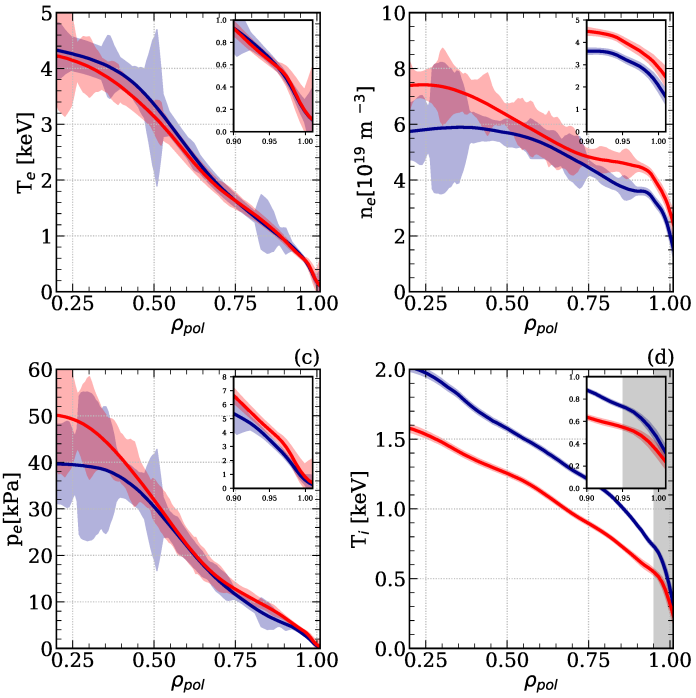

Figure 8. Profiles of the electron temperature (T_e [keV]), electron density (n_e [10^{19}m^{-3}]), electron pressure (p_e [kPa]) and the ion temperature (T_i [keV]) compared between the two discharges # 40470 H-mode in blue and # 40869 H-mode in red. Color coding corresponds to the two discharges with different ion grad B drift - blue in favorable (# 40470) and red in unfavorable configuration (# 4069). The region of large uncertainty in CXRS measurements is enclosed in grey rectangles.

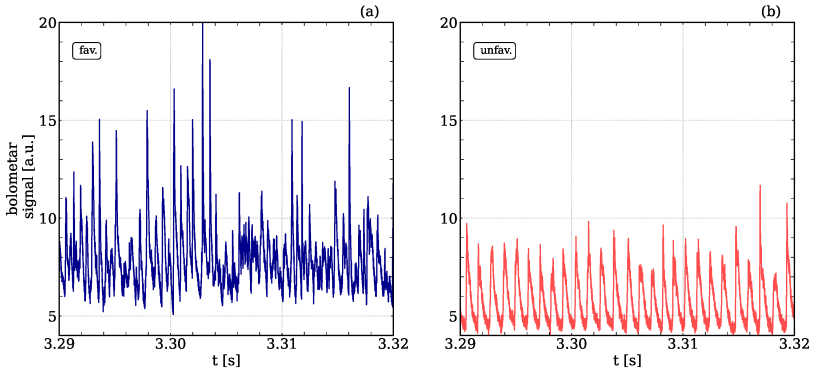

Figure 9. Temporal evolution of ELM frequency showing different regularity of ELMs between fav. (a) and unfav. (b).

figure 4 although in the ECRH case, the edge electron temperature is stronger while the density at the edge in only slightly higher in unfav. discharge. Regardless, in both pairs the separatrix density appears to be higher in unfavorable case and although there are no conclusive statements about the divertor conditions at this point, further studies are planned to investigate the connection between ELMs and separatrix conditions.

The ideal PB stability analysis displayed in figure 10 shows that the experimental

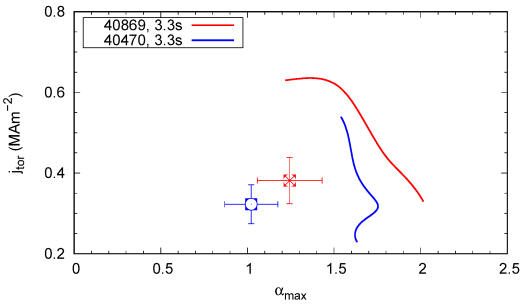

Figure 10. Ideal peeling-ballooning stability diagram for the two cases: favorable shown in blue and unfavorable displayed in red. The experimental points are noted as squares in α_{max}, j_{tor} space, while the solid lines are their respective boundaries computed with varying pressure gradients α_{max} and current densities j_{tor}

points of both favorable and unfavorable case are far away from the boundary as were the ECRH heated discharges shown in figure 5. In this case, the pressure gradients and current densities are slightly higher for unfavorable case but within the uncertanties.

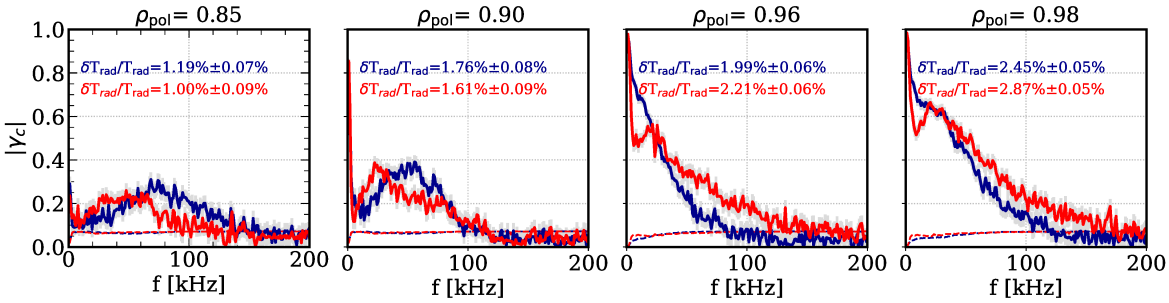

Figure 11. Coherency spectra are calculated by cross-correlating two neighboring correlation ECE channels. They are displayed at four different radial locations inside the pedestal top and towards the separatrix. Color coding corresponds to two discharges with different ion ∇B drift - blue in favorable and red in unfavorable configuration. Associated temperate fluctuations are calculated by integrating the coherency levels in frequency space between 5 - 200 kHz.

Figure 11 shows the coherency spectra obtained with the CECE system at four radial locations, spanning the outer core region towards the separatrix. Color coding corresponds to the two different drift configurations. The outer core channel at $\rho_{\mathrm{pol}} = 0.85$ shows slightly higher fluctuation levels of $1.19\,\% \pm 0.07\,\%$ in favorable compared to $1.00\,\% \pm 0.09\,\%$ in unfavorable similar to the previous observations in the ECRH heated plasmas. The peak frequency is Doppler shifted due to higher toroidal rotation in the favorable discharge. Higher toroidal rotation is the result of the same torque applied to the lower density discharge for the same amount of heating power. In addition, the lower ion orbit losses in favorable compared to unfavorable drift direction might play a role. The spectral shapes and fluctuation levels measured inside the pedestal top at $\rho_{\mathrm{pol}} = 0.90$ show a formation of a peaked structure in the unfavorable discharge. However, the fluctuation levels are similar ($1.76\,\% \pm 0.08\,\%$) in favorable

and $(1.61\,\% \pm 0.09\,\%)$ unfavorable. At the pedestal top location, at $\rho_{\mathrm{pol}} \approx 0.96$, the peaking dominates the spectra in the unfavorable discharge and the fluctuation levels are $2.21\,\% \pm 0.06\,\%$ and are higher compared to favorable case where $\delta T_{\mathrm{rad}}/T_{\mathrm{rad}} = 01.99\,\% \pm 0.026\,\%$. This trend continues towards the steep gradient region at $\rho_{\mathrm{pol}} = 0.98$ where stronger fluctuations are measured in unfavorable $2.87\,\% \pm 0.05\,\%$ compared to favorable $2.45\,\% \pm 0.05\,\%$. Furthermore, we look into the divertor power loads on the outer divertor target in those two discharges as shown in figure 12 as both discharges have good quality IR measurements. Since the ELM frequency is high, no split into an inter-ELM and intra-ELM power load is possible with the available infrared thermography system [39]. We, therefore, analyse ELM averaged divertor power load profiles on the outer divertor target.

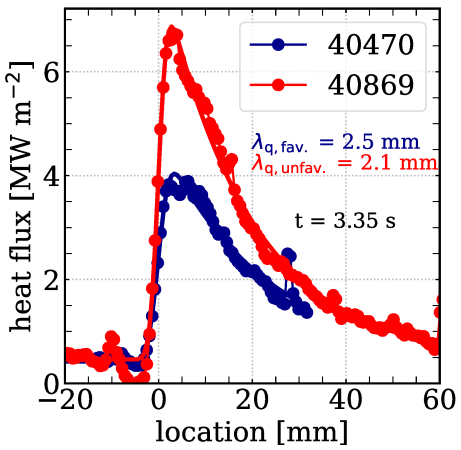

Figure 12. ELM averaged power load profiles on the outer divertor target for the discharge # 40470 in favorable (blue) and unfavorable # 40869 (red) drift direction. Power fall-off length (λ_{q}) is measured to be 2.5 mm in favorable and slightly lower 2.1 mm in unfavorable case.

Both profiles, shown in figure 12 are taken in the steady state phase and averaged over 21 IR profiles (about 30 ms). The two discharges have the same heating power, however, the discharge with favorable drift exhibits higher radiated power (see figure 7 (a)), consistent with the reduced power load onto the divertor shown as a blue solid line in figure 12 and correlates with weaker temperature fluctuations across the pedestal shown in figure 11. Interestingly, the unfav. discharge exhibits a smaller power fall-off length λ_{q} =2.1 mm, and this trend is consistently observed throughout the NT experimental campaign [40]. A similar effect was seen in previous L-mode studies [41]. A potential explanation are magnetic drift effects and the up-down asymmetric plasma cross-section as proposed in [42] following the heuristic drift based model by Goldston [43]. The multi-machine H-mode scaling [44] and the JET-AUG H-mode scaling [45] both predict a power fall-off length of $\lambda_{\mathrm{q}} \approx 2$ mm and this is slightly lower than the measured λ_{q} in the two discharges. However, this is consistent since these scaling law predictions are for the inter-ELM phase and, in general, ELMs have a larger wetted area than the inter-ELM profile [46]. A broader profile could be expected when averaging

small ELMs or filaments, as observed in the quasi continuous exhaust (QCE)regime in ASDEX Upgrade[47].

So far, we conclude that the operation in unfavorable drift direction did not provide means of avoiding the LH transition, however, it provides with further opportunity to explore the physics related to the fav./unfav. H-modes. We also conclude that fav. and unfav. NT discharges have different ELM behavior, despite similar experimental conditions and this behavior is not explained by the PB analysis. While in ECRH discharges it looks like turbulence could be contributing to this behavior, this is not the case with the ECRH + NBI comparison. This also suggests the potential difference in type of turbulence in ECRH and ECRH+NBI heated plasma. In the following, we examine potential for LH transition avoidance through comparison between weak and strong shaped plasma.

2.3. Increased shaping

As demonstrated in DIII-D, stronger shaping provides more resilience to H-mode access [48]. As we have seen in the previous paragraph, the high shaping discharges entered H-mode and in the following we compare one of those discharges - the high shaping discharge in H-mode (# 40870), with a low shaping (# 37388) discharge that maintained L-mode. Aside from shaping, the main difference between the two discharges is that the low shaping discharge was obtained with 600 kA of plasma current while the high shaping H-mode were obtained with $I_\mathrm{p} = 800\,\mathrm{kA}$. Both discharges were in unfavorable drift configuration. Figure 13 displays some of the main parameters of the two discharges where the low shaping discharge parameters are displayed in red and the high shaping discharge parameters in orange. Figure 13 (a) & (b) shows the applied ECRH heating power levels, power radiated from the main chamber P_rad and NBI beam blips P_NBI applied for CXRS measurements of the ion temperature. Slightly higher ECRH power of 3.4 MW is applied in the case of low shaping compared to the high shaping where 3 MW of ECRH heating power were used. As seen in figure 13 (c) & (d), the ELM monitor shows different behavior in the two cases: flat, no ELM signature in low shaping and ELMs in high shaping case. Plasma stored energy is higher in the high shaping case as shown in figure 13 (e) & (f). The electron density at the edge is the same for both cases so is the fuelling displayed in the same panel in figure 13 (g) & (h). The flux surface contours for the two discharges are displayed in figure 13 separately. While the average triangularity of low shaping discharge is $\delta_\mathrm{av} \approx 0$, the average triangularity for the higher shaping discharge is $\delta_\mathrm{av} \approx$ -0.15.

The corresponding profiles of the electron temperature T_e, electron density n_e, electron pressure p_e and the ion temperature T_i are shown in figure 14. They are averaged during the steady state phases shown in figure 13 and compared between discharges with low shaping (# 37388) and the discharge with high shaping (# 40870), both obtained in unfavorable ion ∇B drift direction. Profile shapes differ between the two discharges across the entire radius - the stronger shaping discharge forms a pedestal in the T_e, while the low shaping one remains without pedestal.

The key factor leading to the difference in pedestal behavior and confinement is demonstrated in figure 15, where the $\mathrm{E_r}$ measurements from the Doppler reflectometer (DR) are shown. The working principles and the methodology behind obtaining E_r measurements from DR are described in [49]. As seen, the high shaping discharge has a single data point across the pedestal, implying the E_r well of at least -20 kV/m. This is a deeper E_r well than that obtained in favorable discharge 40473 of about -15 kV/m, also shown for comparison. It is important to note that the uncertainties in the radial position of DR measurements due to the uncertainties in the density profiles can affect the exact location of the measurements. In L-modes, however, it has been reported that the Er well in the confined plasma is shallower in unfavorable compared to the favorable drift configuration [50]. The strong-shaped plasma is clearly in H-mode, characterized by the deep E_r well and strong E_r shear, while the shallow E_r corresponds to the discharges

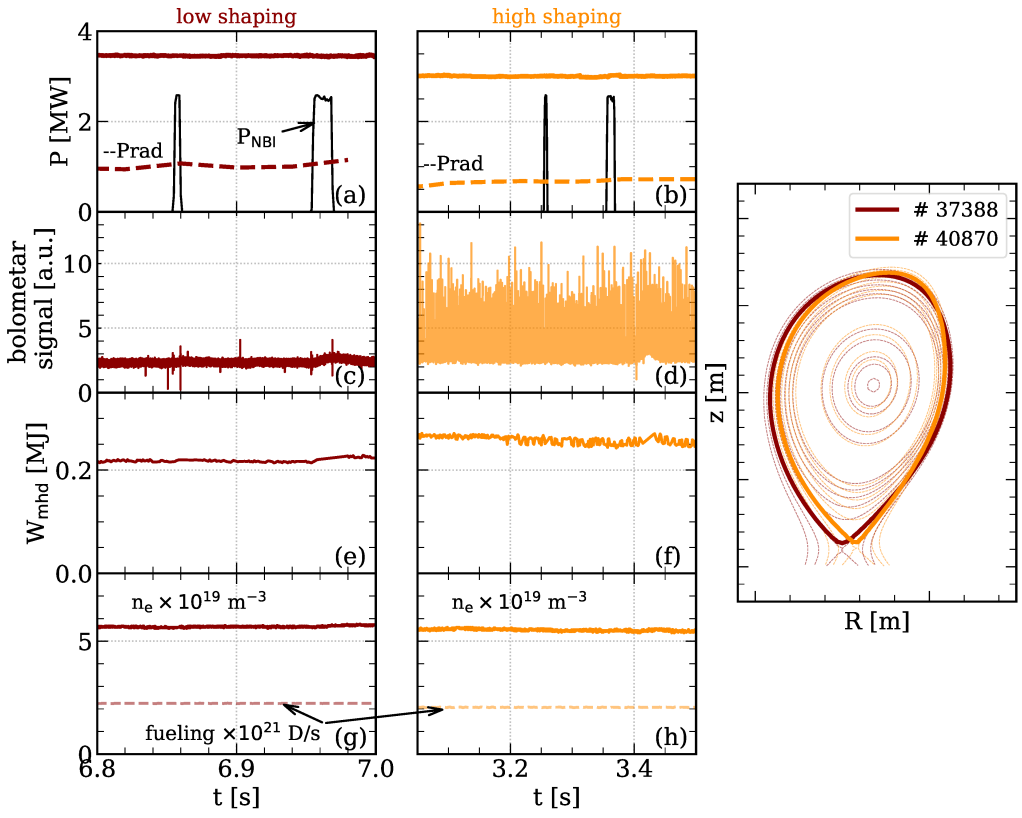

Figure 13. Time histories of different signals compared between low shaping (red) and high shaping (orange) discharges. a,b) Input power. d,c) ELM monitor e,f) H98 g) shapes during the steady state phases.

with weak shaping and is typical of an L-mode despite the slightly higher heating power. Magnitude of the rotation profile in H-mode is higher compared to a flat core rotation profile typical for L-mode plasmas in ASDEX Upgrade [51].

Radial profiles of the relative radiation temperature $\delta T_{\mathrm{rad}}/T_{\mathrm{rad}}$ fluctuation levels, measured with CECE are shown in figure 16 for both L-mode discharge (# 37388) in red and H-mode discharge (# 40870) in orange. The fluctuation levels are calculated by integrating the coherency levels across the frequency range of 5 - 200 kHz. This comparison shows two times higher fluctuation values across the L-mode pedestal region compared to an H-mode, which is consistent with the picture of the lower $E \times B$ shear in L-mode compared to an H-mode. While reduced fluctuations are consistent with increased E_{r} shear, the main remaining question is why stronger shaping plasma enters H-mode and weakly shaping plasma not. A partial response to this question could be the timing of the application of the auxiliary heating. For example, in the discharge with low shaping, the heating is applied after shaping reached its final value at $\delta_{\mathrm{u}} \approx -0.27$. In the high shaping case, the heating was applied very early in the discharge, when $\delta_u \approx$

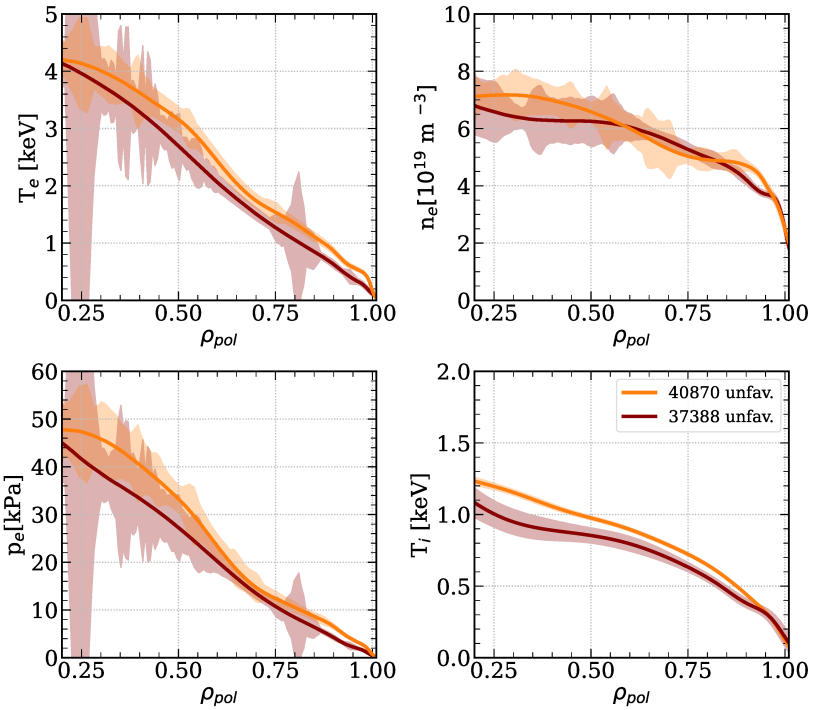

Figure 14. Profiles of the electron temperature (T_e [keV]), electron density (n_e [$10^{19}m^{-1}$]), electron pressure (p_e [kPa]) and the ion temperature (T_i [keV]) compared between the two discharges # 40870 H-mode in orange and # 37388 L-mode in dark red. Both discharges were obtained in unfav. drift direction and similar ECRH heating power levels.

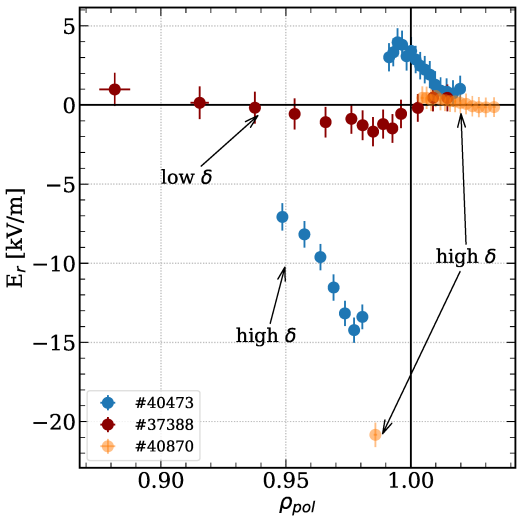

Figure 15. Radial electric field across the pedestal and the scrape-off layer (SOL) as measured by Doppler reflectometry compared between two high shaping discharges, # 40473 in blue and # 40870 in orange, and the low shaping discharge # 37388 in red. The discharge # 40473 shows a pronounced E_r well, typical of H-modes while the shallow E_r well, typical of L-modes (# 37388 in red). is seen. Due to the lack of good quality data, the full E_r well cannot be resolved for the case of # 40870, but a single measurement point in the pedestal indicates the depth of the E_r well could be at least about -20 kV/m.

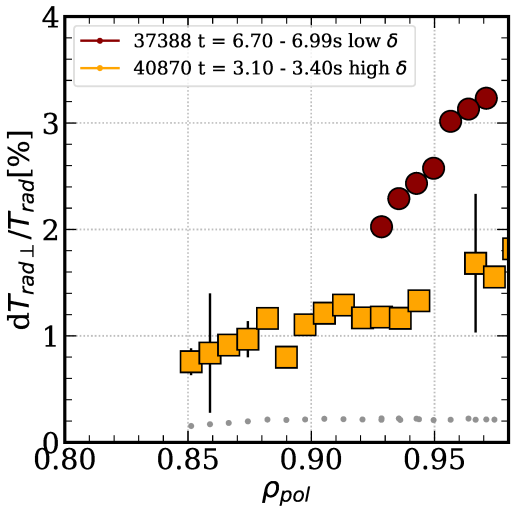

Figure 16. Profile of the radiated temperature fluctuation obtained integrating CECE coherency spectra between 5 - 200 kHz for L-mode in red and H-mode in orange.

-0.04 and throughout the shaping ramp as shown in 17. Important to note that the safety factor (q) profile (not shown) is also changing during this time period. Therefore this early heating during the shaping ramp might have been sufficient to facilitate LH transition and in combination with changing q and with the shape lower than the target shape, the H-mode could not be avoided.

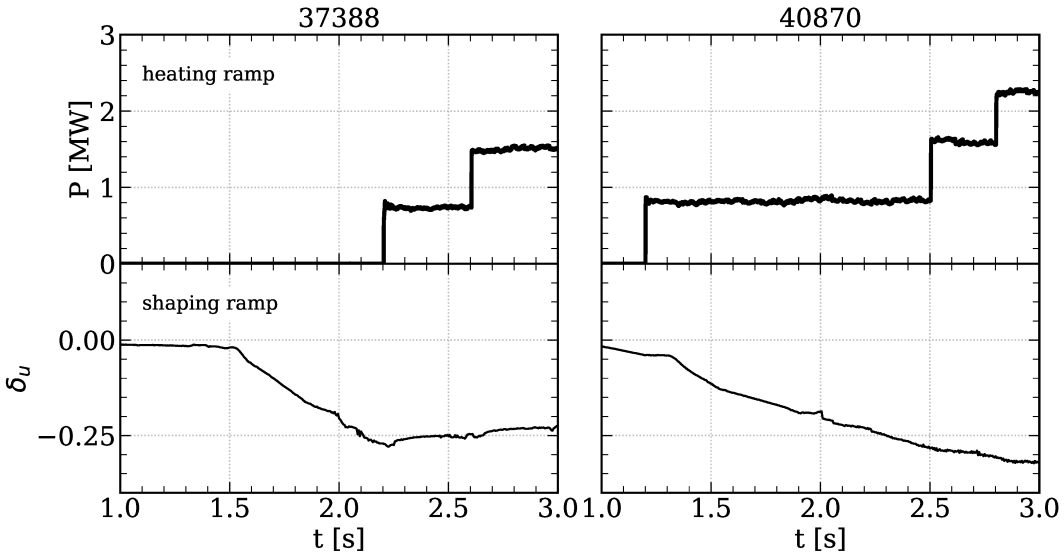

Figure 17. Examples of the heating/shaping time histories at the beginning of the discharges with 600 kA without LH transition to the left and 800 kA where the LH transitions occured, to the right.

Table 1. Operational space of B_t and I_p achieved in ASDEX Upgrade NT campaigns and analyzed in this work.

LSN configuration		
campaign	2020/2021	2022
I_p [kA]	$\pm$ 600	$\pm$ 800
B_t [T]	$\mp$ 2.5	$\mp$2.5

3. AUG NT database and ELM characteristics

In the following, a broader AUG NT database is presented. The discharges span plasma currents of 600 kA and 800 kA with some variation of triangularity. Combination of the two values of I_p and fixed magnetic field provides a conservative variation in edge safety factor q_{95} and magnetic shear s. Table 1 shows combination of B_t and I_p signs and values, used for NT discharges in AUG. The discharges with higher plasma current provided the stabilisation of the fast particles through an increased density (as $n_e \propto I_p$). In addition, with an increased fraction of NBI heating in some of the discharges, to raise the T_i/T_e ratio, the discharges shift towards increasing Ion Temperature Gradient (ITG) as the dominant turbulence regime. The operational space in terms of achieved pedestal pressure and average triangularity observed within the entire AUG NT database is displayed in figure 18. The data points are separated by color-coding into phases with ELMs (in red) and no ELMs (in blue). In addition, a separation of the data points is done through a plasma current - 600 kA are shown in circles and 800 kA in crosses. The relationship between the achieved pedestal top pressure evaluated at $\rho_{pol} = 0.95$ and the upper triangularity is shown in 18 (a) where it can be seen that the majority of blue points and the phases with no ELMs are around weaker upper triangularity of -0.2. Most of those discharges are ran in 600 kA plasma. Contrary to this, the data points at stronger triangularity are mostly H-modes suggesting that there are other parameters besides shaping that dictate the LH threshold in those cases. For example, the early heating during the shaping ramp has already been mentioned as a possible candidate. Furthermore, the separation of the data points with current is also not conclusive. The discharges at stronger shaping were mostly ran at higher plasma current, but this does not affect the achieved pedestal pressures as those are comparable to the discharges at lower plasma current. The electron pedestal pressures of up to 4 kPa are attained across all upper triangularity values and currents.

However, as depicted in Figure 18 (b), in the majority of the cases, the highest volume averaged plasma pressure is achieved during ELMy phases with 800 kA (shown

in red crosses) with the exception of a single data point occupying the upper corner of the parameter space performed at 600 kA of plasma current. The rest of the ELMy discharges at 600 kA (shown in red circles) are around or below their 600 kA no ELM counter-parts shown in blue circles. The volume averaged plasma pressure is computed based on plasma stored energy, as follows: $\bar{p} = (2/3)W_{\mathrm{MHD}}/V$, where W_{MHD} represents the plasma stored energy derived from equilibrium measurements, and V denotes the plasma volume. Furthermore, since most of the discharges transitioned to H-modes with

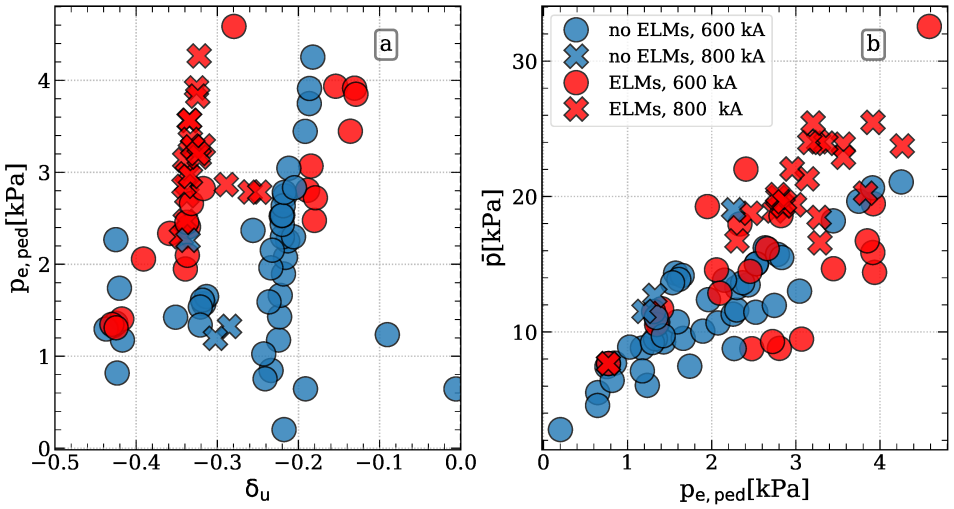

Figure 18. The database showing some of the parameters achieved within the entire database of negative triangularity discharges: a) Achieved electron pedestal pressure at experimentally achieved upper triangularity (δ_u). b) Volume averaged plasma pressure as a function of the electron pedestal pressure. Pedestal pressure is evaluated at $\rho_{\mathrm{pol}} = 0.95$. Blue data points correspond to phases without ELMs, while red points correspond to phases with ELMs. Circles are displaying the discharges obtained at 600 kA while the crosses are denoting 800 kA discharges.

ELMs, characteristics of those ELMs are outlined.

4. Characterisation of ELMs

4.1. ELM Energy losses

Since type-I ELMs are of major concern due to their peak energy loads onto the divertor, it is helpful to compare ELMs appearing in NT plasma with typical type-I ELMs achieved at ASDEX Upgrade in positive triangularity. It is important to note that here we are looking into a mixed data bases consisting of positive triangularity type-I ELMs and negative triangularity ELMs. In addition, we include pedestal relaxation events appearing in I-modes. Figure 19 displays the energy loss per ELM at a given pedestal collisionality for positive triangularity type-I ELMs in red circles, pedestal relaxation events (PREs) [52] in black triangles, and negative triangularity ELMs shown in purple

squares. The energy loss due to an ELM is calculated from the stored plasma energy as $\Delta W_{\mathrm{mhd}}/W_{\mathrm{mhd}}$, and the pedestal collisionality is calculated as defined in [2]:

$$\nu^*_{ped} = 6.9 \times 10^{-18} \frac{R q_{95} Z_{eff} ln\Lambda n_{e,ped}}{\epsilon^{3/2} T^2_{e,ped}} \tag{3}$$

Where R is major radius, $\epsilon = a/R$ is the inverse aspect ratio with a being the minor radius, $n_{\mathrm{e,ped}}$ and $T_{\mathrm{e,ped}}$ are the electron density and temperature evaluated at $\rho_{\mathrm{pol}} = 0.95$, Z_{eff} is the effective ion charge and q_{95} edge safety factor. The Coulomb logarithm for electron-ion collisions at the pedestal top is defined as [53]: $ln\Lambda = 31.3 - ln({n_{\mathrm{e,ped}}}^{1/2} {T_{\mathrm{e,ped}}}^{-1})$.

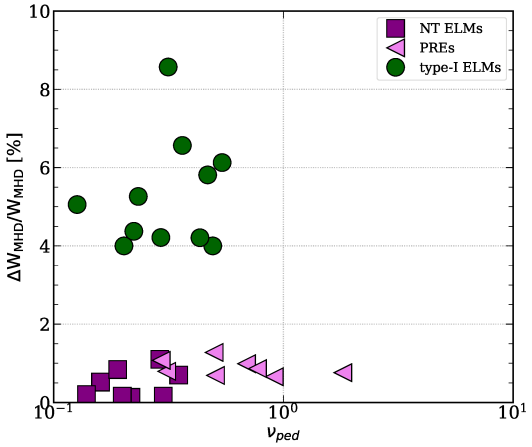

Figure 19. ELM energy loss in % as a function of the pedestal collisionality for type-I ELMs in typical positive triangularity discharges (green circles), pedestal relaxation events appearing in I-modes (violet triangles), and negative triangularity ELMs (purple squares).

While the ELM energy loss of type-I ELMs surpasses 4 %, the ELM energy loss for PREs and NT ELMs are of the order or 1 % and below. PREs appear in I-modes, close to the L-H threshold, and a more comprehensive inter-machine comparison between PREs and type-I ELMs is published in [52]. Low energy losses per ELM have also been reported in TCV negative triangularity experiments [54] and are associated with a strong reduction of the pedestal height and width observed using the EPED model when going from positive to negative triangularity [55].

4.2. ELM frequency

To look for the behavior of ELM frequency response to changing triangularity, a database consisting of the data points from the negative trianglarity data set with ELMs as well as two data points at positive triangularity with type-I ELMs are compared. The result is shown in figure 20. The data shown here corresponds to the phases of the discharges with varying input power levels between 2 and 9 MW. The database contains the discharges with 600 and 800 kA of plasma current as well as the discharges operating in favorable

and unfavorable drift, but as there were no outstanding trends those points are not specifically outlined in the figure, for the sake of clarity. As can be seen in figure 20, as the triangularity decreases, the ELM frequency increases. This trend is seen in blue and light points where power into the plasma was up to 6 MW. This trend is in agreement with trends observed at TCV tokamak [54] and is associated with strong reduction of the pedestal height connected to the closing of the second stable region for ballooning modes [55]. As can be seen in figure 20, at strongest average triangularity, ELM frequencies are grouped around 400 kHz and 800 kHz. The lowest ELM frequency, below 100 Hz, is measured during type-I ELMy H-modes in positive triangularity and those are the two data points at $\delta_a \approx 0.2$. Red points at 800 kHz correspond to the stronger heating phases of the same discharges centered around 400 kHz. This increase in frequency due to the heating power increase is the same as in the case with type-I ELMs. But nevertheless, as seen in Section 2.1, unlike a typical type-I ELMs seen in ASDEX Upgrade, those ELMs do not cross their ideal PB stability boundary.

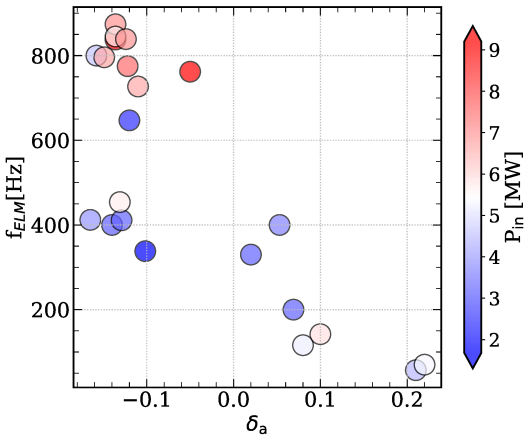

Figure 20. ELM frequency as a function of the average triangularity. Color coded are representing the input power used for the phase where the ELM frequency is evaluated. This data set contains the discharges performed at both 600 and 800 kA of lasma current as well as in both favorable and unfavorable drift direction.

5. Discussion & Conclusion

Two pairs of discharges featuring an upper triangularity of $\delta_u \approx -0.35$ and $I_p = 800\,kA$, subjected to pure ECRH and combined ECRH with NBI heating, were compared between favorable and unfavorable ion ∇B drift configurations. In all cases, the discharges undergo the LH transitions with accompanying ELMs. The frequency of those ELMs increases with power suggesting their type-I nature. Interestingly, comparison of ELMs at matching power levels show irregular frequency patterns in favorable cases, while ELM frequency patterns were regular in those with unfavorable configuration. In addition, frequency patterns seem to correlate with the distance from the LH transition meaning that, just after the LH transition, ELMs in favorable drift direction are also well defined and regular. Extensive studies on ELM behavior and comparison between fav. and unfav. drift direction have not been done, therefore, to understand such behavior, more experiments are needed in particular to connect this behavior to positive triangularity discharges. In literature there are some indications that such behavior takes place. For example, observations in the EAST tokamak in positive triangularity noted occurrences of high-frequency "grassy" ELMs (above 1 kHz) in both drift directions, with the phenomenon of "clustered ELMs" observed in the favorable drift direction [56] and it was indicated that an elongated plasma with a large outer gap and lower electron heating power seems to facilitate the occurrence of clustered grassy ELMs in favorable configuration. However, the physical mechanism behind such behavior remains unknown. Furthermore, recent studies by G. Yu et al [57], where they compare high and low shaped NT plasmas in DIII-D, show similarities to the pure ECRH cases shown here. In the low shaping case they obtain H-modes with clear ELMs while in the high shaping case the discharge remains in L-mode based on the D_α signal showing rather continuous irregular frequency patterns as it was in the pure ECRH fav. case. However, AUG case is in H-mode characterized by the deep Er well, shown in figure 15, used as a confinement qualifier throughout this manuscript.

Ideal PB analysis of the experimental points between ELMs reveals that they are far away from their respective ideal PB stability boundaries. This suggests a different nature of ELMs to those of type-I ELMs, although ELM frequency increases with input power. All discharges display much lower pressure gradient compared to the DIII-D low triangularity case reported in [48]. Triggering of ELM before hitting the PB stability boundary resembles resistive ELMs measured at JET. However, as the resisitvity is not included in ideal PB calculations, statements about type of ELMs in those NT discharges cannot be made. To account for resistivity, future studies with resistive MHD codes are needed. Resistive balooning mode has been identified at DIII-D edge as a potential mechanism for the clamping of the pressure gradient in NT discharges with various degree of triangularity [57].

Further analysis comparing favorable and unfavorable magnetic configurations during ECRH-heated plasma revealed distinct pressure gradient disparities - forward field discharge exhibited a pressure gradient lower than the unfavorable one.

Nevertheless, both discharges fall below their respective ideal PB stability limits. Similarly, in the context of mixed ECRH and NBI heating scenarios, comparable pressure gradients, below their respective ideal PB stability limits are obtained. In all the cases, higher pressure gradient is measured in unfavorable drift direction where ELM frequency patters show regular behavior.

The CECE instrument facilitated insight into pedestal turbulence. In ECRH-heated discharges, a relaxed pressure gradient in the favorable drift direction features increased temperature fluctuations measured by CECE, aligning with a shallower radial electric field (E_r) well and lower E_r shear. Conversely, the unfavorable discharge exhibited lower edge fluctuation levels, likely attributed to a deeper E_r well compared to the favorable configuration. During the steady state of the mixed heating scheme (NBI + ECRH), specific statements about E_r were limited due to inadequate measurement quality. Nevertheless, coherence and temperature fluctuation indicated the emergence of mode-like structures and increase in the fluctuation levels in the unfavorable grad B drift. The IR measurements of the powere fall-off length show that the unfavorable discharge exhibits a smaller λ_q =2.1 mm, and this trend is consistently observed throughout the NT experimental campaign [40]. A similar effect was seen in previous L-mode studies [41] with a potential reason being magnetic drift effects and the up-down asymmetric plasma cross-section as proposed in [42] following the heuristic drift based model by Goldston [43]. The multi-machine H-mode scaling [44] and the JET-AUG H-mode scaling [45] both predict a power fall-off length of $\lambda_q \approx 2$ mm and this is slightly lower than the measured λ_q in the two discharges. However, this is consistent since scaling law predictions are for the inter-ELM phase and a broader profile could be expected when averaging small ELMs or filaments, as observed in the quasi continuous exhaust (QCE)regime in ASDEX Upgrade[47].

A comparison between low and high shaping plasma showed that an increased plasma shaping did not yield ELM avoidance; stronger-shaped plasmas with unfavorable configurations entered H-mode. A comparative analysis between two discharges featuring similar plasma parameters but differing shaping and plasma currents revealed distinct edge profiles and radial electric field characteristics indicative of varied confinement qualities. Lower shaping resembled typical L-mode behavior, whereas higher shaping exhibited H-mode characteristics. CECE data corroborated this observation, showcasing double the fluctuation levels in L-mode compared to H-mode which is consistent with the picture of reduced turbulence in H-mode. However, what is not yet fully understood is why the LH transition occurs in high shaping discharge. Here, it is important to note that the L-mode discharge is performed at lower plasma current compared to the H-mode discharge. Higher plasma current reduces the magnetic shear and for shaped plasmas at low magnetic shear the plasma enters the 2nd stability where the ideal infinite n ballooning mode stability limit for the pressure gradient completely disappears [48]. In addition, it was identified in the numerical study with gyrokinetic code GENE [58] that the negative triangularity has stabilizing effect only when the magnetic shear is high. Therefore, whether the NT will be beneficial or

not highly depends on interplay between triangularity, magnetic shear and possibly other parameters rather than the triangularity alone. For example, the achieved upper triangularities of AUG are marginal and very close to the values that enabled successful NT operation at machines like TCV and DIII-D. Despite those values of triangularity, efforts to attain enhanced confinement similar to reported L-mode-like plasmas in TCV and DIII-D for typical achievable triangularity values at ASDEX Upgrade, have proven unsuccessful thus far. Probing the access to the 2^{nd} stability with infinite-n balooning codes like HELENA and BALLOO of the AUG discharges is currently ongoing. In addition, in high shaping cases, auxiliary plasma heating was initiated during the shaping ramp-up phase, leading to LH transitions occurring at lower shaping compared to the target values.

Furthermore, a database of all NT discharges has been assembled and the highest volume averaged pressures are attained for ELMy discharges obtained at strongest shaping and 800 kA of plasma current. In most instances, discharges transitioned into H-mode accompanied by Edge Localized Modes (ELMs). Notably, the observed ELM energy loss remained at or below 1%, marking a reduction by a factor of 4 compared to type-I ELMs recorded under positive triangularity at identical pedestal collisionality. Additionally, the frequency of ELMs increases with a decrease in average triangularity, reaching values as high as 1 kHz with pronounced negative triangularity. Low energy losses per ELM and the ELM frequency trend with triangularity are consistent with reported TCV negative triangularity experiments [54] and is associated with strong reduction of the pedestal height connected to the closing of the second stable region for ballooning modes [55].

Despite the lack of H-mode avoidance upon transitioning from favorable to unfavorable drift directions, valuable insights were gained into the interplay between MHD macro instabilities and turbulence in negative triangularity plasmas. Given ASDEX Upgrade's limitations in shaping capabilities, further investigations into its shapes compared to tokamaks demonstrating high-quality NT plasmas hold promise in understanding triangularity's impact on H-mode transitions. Employing turbulence codes such as CGYRO could significantly aid in comprehending the turbulence nature in both ECRH and ECRH and NBI plasmas.

6. Acknowledgments

The main author would like to thank Olivier Sauter and Rachael McDermott for constructive criticism of the manuscript, Clemente Angioni for a fruitful discussion and Roxana Takács for forward modelling of the CXRS measurements. This work is supported by the US DOE under Award DE-SC0014264. This work has been carried out within the framework of the EUROfusion Consortium, funded by the European Union via the Euratom Research and Training Programme (Grant Agreement No 101052200 — EUROfusion). Views and opinions expressed are however those of the author(s) only and do not necessarily reflect those of the European Union or the European Commission. Neither the European Union nor the European Commission can be held responsible for them.

[1] H R Wilson, S C Cowley, A Kirk, and P B Snyder. Magneto-hydrodynamic stability of the h-mode transport barrier as a model for edge localized modes: an overview*. *Plasma Physics and Controlled Fusion*, 48(5A):A71, apr 2006.

[2] A Loarte, G Saibene, R Sartori, D Campbell, M Becoulet, L Horton, T Eich, A Herrmann, G Matthews, N Asakura, A Chankin, A Leonard, G Porter, G Federici, G Janeschitz, M Shimada, and M Sugihara. Characteristics of type i elm energy and particle losses in existing devices and their extrapolation to iter. *Plasma Physics and Controlled Fusion*, 45(9):1549, aug 2003.

[3] T. Eich, B. Sieglin, A.J. Thornton, M. Faitsch, A. Kirk, A. Herrmann, and W. Suttrop. Elm divertor peak energy fluence scaling to iter with data from jet, mast and asdex upgrade. *Nuclear Materials and Energy*, 12:84–90, 2017. Proceedings of the 22nd International Conference on Plasma Surface Interactions 2016, 22nd PSI.

[4] H Zohm. Edge localized modes (elms). *Plasma Physics and Controlled Fusion*, 38(2):105, feb 1996.

[5] T. E. Evans, R. A. Moyer, P. R. Thomas, J. G. Watkins, T. H. Osborne, J. A. Boedo, E. J. Doyle, M. E. Fenstermacher, K. H. Finken, R. J. Groebner, M. Groth, J. H. Harris, R. J. La Haye, C. J. Lasnier, S. Masuzaki, N. Ohyabu, D. G. Pretty, T. L. Rhodes, H. Reimerdes, D. L. Rudakov, M. J. Schaffer, G. Wang, and L. Zeng. Suppression of large edge-localized modes in high-confinement diii-d plasmas with a stochastic magnetic boundary. *Phys. Rev. Lett.*, 92:235003, Jun 2004.

[6] M. Greenwald, R. Boivin, P. Bonoli, R. Budny, C. Fiore, J. Goetz, R. Granetz, A. Hubbard, I. Hutchinson, J. Irby, B. LaBombard, Y. Lin, B. Lipschultz, E. Marmar, A. Mazurenko, D. Mossessian, T. Sunn Pedersen, C. S. Pitcher, M. Porkolab, J. Rice, W. Rowan, J. Snipes, G. Schilling, Y. Takase, J. Terry, S. Wolfe, J. Weaver, B. Welch, and S. Wukitch. Characterization of enhanced D high-confinement modes in Alcator C-Mod. *Physics of Plasmas*, 6(5):1943–1949, 05 1999.

[7] D.G. Whyte, A.E. Hubbard, J.W. Hughes, B. Lipschultz, J.E. Rice, E.S. Marmar, M. Greenwald, I. Cziegler, A. Dominguez, T. Golfinopoulos, N. Howard, L. Lin, R.M. McDermott, M. Porkolab, M.L. Reinke, J. Terry, N. Tsujii, S. Wolfe, S. Wukitch, Y. Lin, and the Alcator C-Mod Team. I-mode: an h-mode energy confinement regime with l-mode particle transport in alcator c-mod. *Nuclear Fusion*, 50(10):105005, oct 2010.

[8] J. Stober, M. Maraschek, G.D. Conway, O. Gruber, A. Herrmann, A.C.C. Sips, W. Treutterer, H. Zohm, and ASDEX Upgrade Team. Type ii elmy h modes on asdex upgrade with good confinement at high density. *Nuclear Fusion*, 41(9):1123, sep 2001.

[9] E. Viezzer, M.E. Austin, M. Bernert, K.H. Burrell, P. Cano-Megias, X. Chen, D.J. Cruz-Zabala, S. Coda, M. Faitsch, O. Février, L. Gil, C. Giroud, T. Happel, G.F. Harrer, A.E. Hubbard,

J.W. Hughes, A. Kallenbach, B. Labit, A. Merle, H. Meyer, C. Paz-Soldan, P. Oyola, O. Sauter, M. Siccinio, D. Silvagni, and E.R. Solano. Prospects of core–edge integrated no-elm and small-elm scenarios for future fusion devices. *Nuclear Materials and Energy*, 34:101308, 2023.

[10] S Coda, A Merle, O Sauter, L Porte, F Bagnato, J Boedo, T Bolzonella, O Février, B Labit, A Marinoni, A Pau, L Pigatto, U Sheikh, C Tsui, M Vallar, and T Vu. Enhanced confinement in diverted negative-triangularity l-mode plasmas in TCV. *Plasma Physics and Controlled Fusion*, 64(1):014004, dec 2021.

[11] M. E. Austin, A. Marinoni, M. L. Walker, M. W. Brookman, J. S. deGrassie, A. W. Hyatt, G. R. McKee, C. C. Petty, T. L. Rhodes, S. P. Smith, C. Sung, K. E. Thome, and A. D. Turnbull. Achievement of reactor-relevant performance in negative triangularity shape in the diii-d tokamak. *Phys. Rev. Lett.*, 122:115001, Mar 2019.

[12] Y Camenen, A Pochelon, A Bottino, S Coda, F Ryter, O Sauter, R Behn, T P Goodman, M A Henderson, A Karpushov, L Porte, and G Zhuang. Electron heat transport in shaped TCV l-mode plasmas. *Plasma Physics and Controlled Fusion*, 47(11):1971–1987, oct 2005.

[13] Y Camenen, A Pochelon, R Behn, A Bottino, A Bortolon, S Coda, A Karpushov, O Sauter, G Zhuang, and the TCV team. Impact of plasma triangularity and collisionality on electron heat transport in TCV l-mode plasmas. *Nuclear Fusion*, 47(7):510–516, jun 2007.

[14] M. Fontana, L. Porte, S. Coda, and O. Sauter and. The effect of triangularity on fluctuations in a tokamak plasma. *Nuclear Fusion*, 58(2):024002, dec 2017.

[15] A Marinoni, S Brunner, Y Camenen, S Coda, J P Graves, X Lapillonne, A Pochelon, O Sauter, and L Villard. The effect of plasma triangularity on turbulent transport: modeling TCV experiments by linear and non-linear gyrokinetic simulations. *Plasma Physics and Controlled Fusion*, 51(5):055016, mar 2009.

[16] J. M. Duff, B. J. Faber, C. C. Hegna, M. J. Pueschel, and P. W. Terry. Effect of triangularity on ion-temperature-gradient-driven turbulence. *Physics of Plasmas*, 29(1):012303, 01 2022.

[17] Gabriele Merlo, Mattia Dicorato, Bryce Allen, Tilman Dannert, Kai Germaschewski, and Frank Jenko. On the effect of negative triangularity on ion temperature gradient turbulence in tokamaks. *Physics of Plasmas*, 30(10):102302, 10 2023.

[18] A.O. Nelson, C. Paz-Soldan, and S. Saarelma. Prospects for h-mode inhibition in negative triangularity tokamak reactor plasmas. *Nuclear Fusion*, 62(9):096020, aug 2022.

[19] A. O. Nelson, L. Schmitz, C. Paz-Soldan, K. E. Thome, T. B. Cote, N. Leuthold, F. Scotti, M. E. Austin, A. Hyatt, and T. Osborne. Robust avoidance of edge-localized modes alongside gradient formation in the negative triangularity tokamak edge. *Phys. Rev. Lett.*, 131:195101, Nov 2023.

[20] S.Yu. Medvedev, M. Kikuchi, L. Villard, T. Takizuka, P. Diamond, H. Zushi, K. Nagasaki, X. Duan, Y. Wu, A.A. Ivanov, A.A. Martynov, Yu.Yu. Poshekhonov, A. Fasoli, and O. Sauter. The negative triangularity tokamak: stability limits and prospects as a fusion energy system. *Nuclear Fusion*, 55(6):063013, may 2015.

[21] M. Kikuchi, T. Takizuka, S. Medvedev, T. Ando, D. Chen, J.X. Li, M. Austin, O. Sauter, L. Villard, A. Merle, M. Fontana, Y. Kishimoto, and K. Imadera. L-mode-edge negative triangularity tokamak reactor. *Nuclear Fusion*, 59(5):056017, apr 2019.

[22] Cheng-Xi Zhou, Jia-Le Chen, V.S. Chan, Xiang Jian, G. Zhuang, and Yi-Ren Zhu and. Effects of triangularity on the fusion performance of CFETR. *Nuclear Fusion*, 60(9):096029, aug 2020.

[23] J.A. Schwartz, A.O. Nelson, and E. Kolemen. To dee or not to dee: costs and benefits of altering the triangularity of a steady-state DEMO-like reactor. *Nuclear Fusion*, 62(7):076006, may 2022.

[24] O. Sauter. Geometric formulas for system codes including the effect of negative triangularity. *Fusion Engineering and Design*, 112:633–645, 2016.

[25] Olivier Sauter. Negative triangularity tokamak operation in tcv. *IAEA conference proceedings*, 2023.

[26] Tim Happel, Thomas Pütterich, Daniel Told, Michael G Dunne, Rainer Fischer, Joerg Hobirk, Rachael M McDermott, Ulrike Plank, and The ASDEX Upgrade Team. Overview of initial negative triangularity plasma studies on the asdex upgrade tokamak. *Nuclear Fusion*, 2022.

[27] P. David, M. Bernert, T. Pütterich, C. Fuchs, S. Glöggler, T. Eich, and the ASDEX Upgrade Team. Optimization of the computation of total and local radiated power at asdex upgrade. *Nuclear Fusion*, 61(6):066025, may 2021.

[28] R. Fischer and A. Dinklage. The concept of Integrated Data Analysis of complementary experiments. *AIP Conference Proceedings*, 954(1):195–202, 11 2007.

[29] R. Takács. Development and application of forward model for cxrs measurements on the ASDEX Upgrade tokamak, 2024.

[30] M G Dunne, S Potzel, F Reimold, M Wischmeier, E Wolfrum, L Frassinetti, M Beurskens, P Bilkova, M Cavedon, R Fischer, B Kurzan, F M Laggner, R M McDermott, G Tardini, E Trier, E Viezzer, M Willensdorfer, The EUROfusion MST1 Team, and The ASDEX-Upgrade Team. The role of the density profile in the asdex-upgrade pedestal structure. *Plasma Physics and Controlled Fusion*, 59(1):014017, oct 2016.

[31] R Sartori, G Saibene, L D Horton, M Becoulet, R Budny, D Borba, A Chankin, G D Conway, G Cordey, D McDonald, K Guenther, M G von Hellermann, Yu Igithkanov, A Loarte, P J Lomas, O Pogutse, and J Rapp. Study of type iii elms in jet. *Plasma Physics and Controlled Fusion*, 46(5):723, mar 2004.

[32] H. Nyström, L. Frassinetti, S. Saarelma, G.T.A. Huijsmans, C. Perez von Thun, C.F. Maggi, J.C. Hillesheim, and JET contributors. Effect of resistivity on the pedestal mhd stability in jet. *Nuclear Fusion*, 62(12):126045, oct 2022.

[33] M. Bornatici, R. Cano, O. De Barbieri, and F. Engelmann. Electron cyclotron emission and absorption in fusion plasmas. *Nuclear Fusion*, 23(9):1153, sep 1983.

[34] W. Suttrop and A. G. Peeters. Practical limitations to plasma edge electron temperature measurements by radiometry of electron cyclotron emission. Technical report, IPP No. 1/306, 1997.

[35] S S Denk, R Fischer, H M Smith, P Helander, O Maj, E Poli, J Stober, U Stroth, W Suttrop, E Westerhof, and M Willensdorfer and. Analysis of electron cyclotron emission with extended electron cyclotron forward modeling. *Plasma Physics and Controlled Fusion*, 60(10):105010, sep 2018.

[36] Vanovac, B., Denk, S.S., Wolfrum, E., Willensdorfer, M., Suttrop, W., Fischer, R., Luhmann, N.C., and ASDEX Upgrade Team. Mode analysis limitations of ece-i & ece measurements at the plasma edge. *EPJ Web Conf.*, 203:02011, 2019.

[37] S. J. Freethy, G. D. Conway, I. Classen, A. J. Creely, T. Happel, A. Köhn, B. Vanovac, and A. E. White. Measurement of turbulent electron temperature fluctuations on the asdex upgrade tokamak using correlated electron cyclotron emission. *Review of Scientific Instruments*, 87(11):11E102, 2016.

[38] A. J. Creely, S. J. Freethy, W. M. Burke, G. D. Conway, R. Leccacorvi, W. C. Parkin, D. R. Terry, and A. E. White. Correlation electron cyclotron emission diagnostic and improved calculation of turbulent temperature fluctuation levels on asdex upgrade. *Review of Scientific Instruments*, 89(5):053503, 2018.

[39] B. Sieglin, M. Faitsch, A. Herrmann, B. Brucker, T. Eich, L. Kammerloher, and S. Martinov. Real time capable infrared thermography for ASDEX Upgrade. *Review of Scientific Instruments*, 86(11):113502, 2015.

[40] K. Lee. Power load investigation in negative triangularity ASDEX Upgrade, 2022.

[41] M Faitsch, B Sieglin, T Eich, H J Sun, A Herrmann, and the ASDEX Upgrade Team. Change of the scrape-off layer power width with the toroidal B-field direction in ASDEX Upgrade. *Plasma Physics and Controlled Fusion*, 57(7):075005, 2015.

[42] M Faitsch, R Maurizio, A Gallo, S Coda, T Eich, B Labit, A Merle, H Reimerdes, B Sieglin, C Theiler, the Eurofusion MST1 Team, and the TCV Team. Dependence of the l-mode scrape-off layer power fall-off length on the upper triangularity in tcv. *Plasma Physics and Controlled Fusion*, 60(4):045010, mar 2018.

[43] R. J. Goldston. Heuristic drift-based model of the power scrape-off width in low-gas-puff H-mode

tokamaks. *Nuclear Fusion*, 52(1):013009, 2012.

[44] T. Eich, A.W. Leonard, R.A. Pitts, W. Fundamenski, R.J. Goldston, T.K. Gray, A. Herrmann, A. Kirk, A. Kallenbach, O. Kardaun, A.S. Kukushkin, B. LaBombard, R. Maingi, M.A. Makowski, A. Scarabosio, B. Sieglin, J. Terry, A. Thornton, ASDEX Upgrade Team, and JET EFDA Contributors. Scaling of the tokamak near the scrape-off layer H-mode power width and implications for ITER. *Nuclear Fusion*, 53(9):093031, 2013.

[45] T. Eich, B. Sieglin, A. Scarabosio, W. Fundamenski, R. J. Goldston, and A. Herrmann. Inter-ELM power decay length for JET and ASDEX Upgrade: Measurement and comparison with heuristic drift-based model. *Physical Review Letters*, 107:215001, 2011.

[46] A. Herrmann, T. Eich, S. Jachmich, M. Laux, P. Andrew, A. Bergmann, A. Loarte, G. Matthews, J. Neuhauser, ASDEX Upgrade team, and Contributors to EFDA-JET work programme. Stationary and transient divertor heat flux profiles and extrapolation to iter. *Journal of Nuclear Materials*, 313-316:759–767, 2003. Plasma-Surface Interactions in Controlled Fusion Devices 15.

[47] M. Faitsch, T. Eich, G.F. Harrer, E. Wolfrum, D. Brida, P. David, M. Griener, and U. Stroth. Broadening of the power fall-off length in a high density, high confinement h-mode regime in ASDEX Upgrade. *Nuclear Materials and Energy*, 26:100890, 2021.

[48] S Saarelma, M E Austin, M Knolker, A Marinoni, C Paz-Soldan, L Schmitz, and P B Snyder. Ballooning instability preventing the h-mode access in plasmas with negative triangularity shape on the diii–d tokamak. *Plasma Physics and Controlled Fusion*, 63(10):105006, sep 2021.

[49] T. Happel, A Bañón Navarro, G. D. Conway, C. Angioni, M. Bernert, M. Dunne, E. Fable, B. Geiger, T. Görler, F. Jenko, R. M. McDermott, F. Ryter, U. Stroth, and the ASDEX Upgrade Team. Core turbulence behavior moving from ion-temperature-gradient regime towards trapped-electron-mode regime in the asdex upgrade tokamak and comparison with gyrokinetic simulation. *Phys. Plasmas*, 22(3):032503, 2015.

[50] U. Plank, D. Brida, G. D. Conway, T. Happel, A. E. Hubbard, T. Pütterich, C. Angioni, M. Cavedon, R. Dux, T. Eich, R. Fischer, P. Hennequin, and ASDEX Upgrade Team. Experimental study of the edge radial electric field in different drift configurations and its role in the access to H-mode at ASDEX Upgrade. *Physics of Plasmas*, 30(4):042513, 04 2023.

[51] R.M. McDermott, C. Angioni, G.D. Conway, R. Dux, E. Fable, R. Fischer, T. Pütterich, F. Ryter, E. Viezzer, and the ASDEX Upgrade Team. Core intrinsic rotation behaviour in asdex upgrade ohmic l-mode plasmas. *Nuclear Fusion*, 54(4):043009, mar 2014.

[52] D. Silvagni, J.L. Terry, W. McCarthy, A.E. Hubbard, T. Eich, M. Faitsch, L. Gil, T. Golfinopoulos, G. Grenfell, M. Griener, T. Happel, J.W. Hughes, U. Stroth, E. Viezzer, the ASDEX Upgrade Team, and the EUROfusion MST1 Team. I-mode pedestal relaxation events in the alcator c-mod and asdex upgrade tokamaks. *Nuclear Fusion*, 62(3):036004, jan 2022.

[53] Mitsuru Honda. Coulomb logarithm formulae for collisions between species with different temperatures. *Japanese Journal of Applied Physics*, 52(10R):108002, sep 2013.

[54] Antoine POCHELON, Paolo ANGELINO, Roland BEHN, Stephan BRUNNER, Stefano CODA, Nataliya KIRNEVA, Sergei Yu MEDVEDEV, Holger REIMERDES, Jonathan ROSSEL, Olivier SAUTER, Laurent VILLARD, Dávid WÁGNER, Alberto BOTTINO, Yann CAMENEN, Gustavo P. CANAL, Prabal K. CHATTOPADHYAY, Basil P. DUVAL, Ambrogio FASOLI, Timothy P. GOODMAN, Sébastien JOLLIET, Alexander KARPUSHOV, Benoît LABIT, Alessro MARINONI, Jean-Marc MORET, Andreas PITZSCHKE, Laurie PORTE, Mikael RANCIC, Victor S. UDINTSEV, and the TCV Team. Recent tcv results - innovative plasma shaping to improve plasma properties and insight. *Plasma and Fusion Research*, 7:2502148–2502148, 2012.

[55] A Merle, O Sauter, and S Yu Medvedev. Pedestal properties of h-modes with negative triangularity using the EPED-CH model. *Plasma Physics and Controlled Fusion*, 59(10):104001, aug 2017.

[56] Genfan DING, Qingquan YANG, Guosheng XU, Xin LIN, Yang YE, Ran CHEN, Yumin WANG, Qing ZANG, Heng LAN, Liang CHEN, Zhikang LU, Yifeng WANG, Lingyi MENG, and Liang WANG. Comparison of natural grassy elm behavior in favorable/unfavorable bt in east. *Plasma*

Science and Technology, 23(9):095105, jul 2021.

[57] G. Yu, Z. Li, G. Kramer, F. Scotti, A. O. Nelson, A. Diallo, C. Lasnier, M. E. Austin, X. Qin, Y. Chen, Y. Zheng, Y. Zhu, and Jr. Luhmann, N. C. Understanding the negative triangularity ELM trigger and ELM free state on DIII-D with ECE-imaging. *Physics of Plasmas*, 30(6):062505, 06 2023.

[58] Gabriele Merlo and Frank Jenko. Interplay between magnetic shear and triangularity in ion temperature gradient and trapped electron mode dominated plasmas. *Journal of Plasma Physics*, 89(1):905890104, 2023.